Investigation of shear rates of rolling adhesion on leukocytes with bending of microvilli

Tai-Hsien Wu* and Dewei Qi†
Department of Chemical and Paper Engineering, Western Michigan University, Kalamazoo, Michigan 49009, USA

(Received 26 October 2018; published 5 June 2019)

An advanced leukocyte model based on a lattice-Boltzmann lattice-spring model (LLM) and an adhesive dynamics (AD) is presented. In principle, the model can deal with not only extensional and compressional but also bending deformation of microvilli of of leukocytes. In this work, the model is applied to investigate how different flow shear rates affect bending deformation of the microvilli and related physical properties. It is demonstrated that at each given flexural stiffness, adhesive bond force, rolling velocity, contact area, number of bonds, and bending deformation increase as the shear rate increases. At each given shear rate, the bending angles of microvilli increase as the flexural stiffness decreases. Therefore, the adhesive bond force, contact area, and number of bonds increase and result in a decrease in cell rolling velocity. The degree of the decrease depends on both shear rate and flexural stiffness. In addition, a bonding and debonding process for individual microvilli is observed and explored from a bending angular point of view.

DOI: 10.1103/PhysRevFluids.4.063101

I. INTRODUCTION

It has been widely acknowledged that further understanding of cell adhesion (e.g., leukocyte rolling adhesion) can help us gain more knowledge about the causes of relevant diseases and may lead to more effective treatments and diagnoses for diseases. Cell adhesion plays important roles in various *in vivo* and *in vitro* binding applications. For example, chimeric antigen receptor T-cells rely on binding to cancer cells, under various shear rates, in order to slow or halt potential cancer growth [1,2]. A more general example is leukocytes rolling along the inflammation-activated vascular endothelium in blood flow, which is a part of the human immune response. This rolling process is mediated by selectin-ligand bonds, such as P-selectin–P-selectin glycoprotein ligand-1 (PSGL-1) bonds. Many experimental and numerical studies have confirmed that the dynamics of adhesion are mainly mediated by the physical chemistry of adhesion molecules, such as the association and dissociation rates of adhesion bonds [3,4], selectin-ligand density, and the local circulatory environment including flow shear rate [3,5].

In the earliest attempts of simulation, leukocytes were modeled by rigid spheres. However, cellular material properties such as cell deformation play a crucial role in the dynamics of cell adhesion. Khismatullin and Truskey [6,7] first used a compound viscoelastic drop to model neutrophils and monocytes to investigate the effects of cell deformability in a parallel-plate flow chamber. Almost at the same time, Jadhav *et al.* [8] used a neo-Hookean membrane as a leukocyte, coupled with the immersed boundary method (IBM), to investigate the influence of cell deformability on leukocyte

*Present address: University of North Carolina at Chapel Hill, Department of Oral and Craniofacial Health Sciences, Chapel Hill, North Carolina 27599, USA; taihsien@email.unc.edu
†Corresponding author: dewei.qi@wmich.edu

rolling adhesion. Their results indicated that cells with deformations roll much slower and are relatively more stable than those without deformation in shear flow, and the results were consistent with the experimental findings [9,10]. Since then numerous simulation studies continue to address the process of cell deformation during cellular adhesion [11–16].

Another critical cellular property is microvillus deformation. Microvilli are fingerlike projections on the surface of leukocytes. Since most adhesion molecules (e.g., PSGL-1) are located at the tips of microvilli, microvillus deformation also affects cellular adhesion. Hence, several simulation studies were performed to examine the influence of the extensional deformation of microvilli on the dynamics of cell adhesion. Khismatullin and Truskey [6] combined the microvillus spring with the receptor-ligand bond spring to express the total extensional deformation of microvilli and adhesive bonds. Later Caputo and Hammer [17] improved Hammer and Apte's pioneering adhesive dynamics (AD) [3] by using an elastic spring and a viscous model to approximate the microvilli elastic and viscous responses to a small force and a large force, respectively. A linear elastic extensional model was used for the small force, while a nonlinear plastic extensional model was created for the large force in a tether regime discovered experimentally by Shao *et al.* [18]. Pawar *et al.* [19] further improved Caputo and Hammer's model by replacing the hard spherical body with a deformable neo-Hookean membrane. Recently Pospieszalska *et al.* combined the existing model for microvillus tether formation with a Kelvin-Voigt viscoelastic model for microvillus extension [20,21]. However, these studies were limited to microvillus extensional deformation, set flexural stiffness essentially equal to zero, and did not consider the bending or compressional deformation.

In fact, when a force tangential to the cell surface is exerted on a leukocyte microvillus, it will be bent. This phenomenon was observed in experiments [22]. Similar to the extensional deformation of microvilli, the bending of microvilli due to their flexibility can potentially influence the binding between selectins and ligands. Munn *et al.* [23] suggested that when microvilli are flattened along the cell surface, the receptors at the bases of microvilli (instead of at the tips of microvilli) may obtain additional adhesion with ligands on the endothelial cells or on the ligand-coated substrate. While Pospieszalska *et al.* first simulated the pivoting of microvilli around their bases, they did not address the flexural stiffness of microvilli [20,21]. Based on the importance of flexibility in microvilli, Yao and Shao [24,25] experimentally measured the flexural stiffness of the microvilli on lymphocytes and neutrophils under small deformation of the microvilli. They reported that the values of the flexural stiffness of lymphocyte and neutrophil microvilli are 4 pN/μm and 7 pN/μm, respectively [24,25]. Simon *et al.* [26] conducted another experiment to measure the flexural stiffness of neutrophil microvilli under a large deformation (0.5–1 μm) and found that the flexural stiffness is 5 pN/μm.

To take account of the bending effects of microvilli, employing the measured data of microvillus flexural stiffness identified by Yao and Shao [24,25], Wu and Qi [27] recently used the immersed boundary lattice-Boltzmann lattice-spring model (LLM) combined with adhesive dynamics simulations [3] to study the roles of flexural stiffness in cell rolling and adhesion at a shear rate of $\gamma = 50\ \mathrm{s}^{-1}$. The results showed that the flexural stiffness has a profound effect on rolling velocity and adhesion bonding force. In their studies, they decomposed each individual adhesion bonding force into two local coordinate-based components: parallel (for extension) and perpendicular (for bending). Their findings revealed that the increasing total local coordinate-based adhesion bonding force is mainly due to an increase in the perpendicular component. The flexibility of microvilli aids not only in expediting contact frequency with the substrate, but also in flattening of microvilli once the contact is established. As a result, the flexibility facilitates the formation of adhesive bonds, confirming the speculation of Munn *et al.* [23].

Unlike the previous work where the shear rate is fixed, now we focus on how different shear rates affect the bending deformation of microvilli, adhesive forces, and rolling velocities. This information is not currently available in literature to the best of our knowledge. IWe show that rolling velocity increases as either the shear rate or flexural stiffness of microvilli increases. However, the net velocity increase due to the flexural stiffness is larger in a large shear rate range than in a smaller shear rate range.

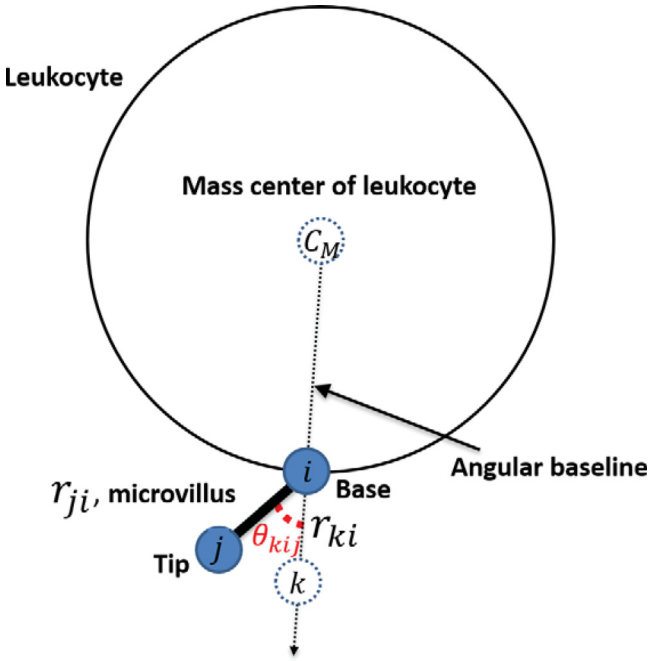

FIG. 1. A microvillus is modeled by a spring with its end fixed at the base node i on the cell surface. The tip node j can be extended or compressed with respect to the base node i. In addition, the vector $\mathbf{r}_{ji}$ can be bent with respect to vector $\mathbf{r}_{ki}$ to have a bending angle θ_{kij}, where the node k is always located on the extension portion of the line connecting the mass center C_M to the base node i.

The same method as that used by Wu and Qi [27] is adopted in the present work. This method comprises five numerical models: (1) lattice-Boltzmann method (LBM) for the Navier-Stokes flow [28–37]; (2) coarse-grained cell model (CGCM) for the viscoelastic leukocyte membrane [13,38–41]; (3) lattice spring model (LSM) for the flexible microvilli [42]; (4) immersed boundary method (IBM) for the fluid-cell interactions [43]; and (5) adhesive dynamics (AD) for stochastic binding between P-selectin and PSGL-1 [3]. A summery of the method with each model is presented in detail in the next section and in the Appendix. The method can deal with not only extensional and compressional but also bending deformation of microvilli of cells.

II. COMPUTATION METHOD

A lattice-Boltzmann LLM [27,42,44–46] combined with the AD is employed. In this method, the LBM is used as a fluid solver to simulate the Navier-Stoke flows, the CGCM [38] is utilized to simulate motion of leukocytes, and the LSM [27] is exploited to mimic the deformation of microvilli while the fluid-solid interactions are treated by IBM. Further, the AD is employed to obtain the adhesive bonding forces between leukocytes and selectin-coated substrates. The LBM, IBM, and CGCM are presented in detail in the Appendix.

A. Lattice spring model

Wu and Qi [27] applied the LSM [42] to mimic the deformation of the leukocyte microvilli. As shown in Fig. 1, a microvillus is modeled by a spring (vector $\mathbf{r}_{ji}$) with its end fixed at the base grid i on the cell surface and with the other end j as the microvillus tip. Note that the base grids in the LSM are also the solid grids in the CGCM. There are two types of deformation of microvilli. First, the tip grid j of the spring can be extended or compressed with respect to the base grid i. The

potential energy between grids i and j responsible for the spring extension or compression U^s_{ji} is given by

$$U^s_{ji} = \tfrac{1}{2}k^{mv}_s(r_{ji} - r_{0ji})^2, \tag{1}$$

where r_{ji} and r_{0ji} are the instantaneous and initial microvillus lengths, respectively, and k^{mv}_s is the extensional spring constant. Note that each microvillus has the same initial length (i.e., $r_{0ji} = L_{mv}$, where $L_{mv} = 0.35$ μm is the average experimental value of the microvillus length).

Second, vector $\mathbf{r}_{ji}$ can be bent with respect to vector $\mathbf{r}_{ki}$ to have a bending angle θ_{kij}, where k is always located on the extension portion of the line connecting the mass center C_M to the base grid i. The line is called the angular baseline (the dashed line in Fig. 1) and is used for the measurement of the bending angle only. Assume that the cell body is spherical initially, then the baseline is overlapped with the radius of the sphere. As the spherical cell is deformed under flow shear forces, it may become, for example, an ellipsoid, and the baseline is gradually separated from the radius of the sphere. Thus, the villus angle with respect to the radius of the sphere equal to zero becomes nonzero with respect to the baseline of the ellipsoid, and even the villi orientation is fixed in space. Therefore, the cell deformation itself causes a change of the angle. Further, hydrodynamic and adhesive forces may cause additional change of angle. This latter portion is purely bending by villus itself. $\mathbf{r}_{ki}$ is the baseline, and there is an ignored force on point k since the mass of the cell is much larger than that of microvillus. The energy due to the bent bond U^a_{kij} is written by

$$U^a_{kij} = \tfrac{1}{2}k^{mv}_a(\theta_{kij} - \theta_{0kij})^2, \tag{2}$$

where k^{mv}_a is the angular spring constant, and θ_{0kij} represents the equilibrium angle, as shown in Fig. 1. The elastic forces due to the extensional and bending deformation are calculated from the negative gradient of the sum of U^a_{ji} and U^s_{kij} with respect to solid grids i and j.

Base on previous experimental measurements and numerical studies [9,24–26], the extensional stiffness and flexural stiffness of the microvilli are 152–1340 pN/μm and 4–7 pN/μm, respectively. The extensional stiffness K^E is directly equal to the spring constant k^{mv}_s, while the flexural stiffness K is defined by a ratio of the force on the microvillus to the corresponding deflection, and it is related to the angular spring constant by $K = k^{mv}_a/L^2_{mv}$ [27]. All parameters used in the LSM are given in Tables I and II.

B. Adhesive dynamics

The AD was first presented in a simulation of leukocyte adhesion to endothelial cells by Hammer and Apte [3]. This method uses the stochastic Monte Carlo method coupled with kinetics models to simulate the formation and rupture of the receptor-ligand bond.

The kinetics model used in this study is the Dembo model [47], where the forward and reverse rates for the receptor-ligand bond are written as

$$k_f = k^0_f \exp\left[-\frac{\sigma_{ts}(l - l_0)^2}{2K_BT}\right], \tag{3}$$

$$k_r = k^0_r \exp\left[\frac{(\sigma_b - \sigma_{ts})(l - l_0)^2}{2K_BT}\right], \tag{4}$$

where k^0_f and k^0_r are the unstressed reaction rates; l and l_0 are the stretched and unstressed equilibrium bond lengths, respectively; σ_b and σ_{ts} are the spring constants in the bound and transition states, respectively; K_B is the Boltzmann constant; and T is the absolute temperature. The adhesive force F_b, acting on the receptor-ligand bond, is assumed to follow the Hookean spring model, which

TABLE I. The simulation dimensional parameters used in this study.

Parameter	Definition	Value (Experimental range)	Reference
ρ_f	Fluid density	1000 kg/m^3	[48]
μ_f	Fluid dynamic viscosity	0.0012 N · s/m^2	[48]
h	Lattice spacing	0.5326 μm	–
δt	Lattice unit of time	0.1512 μs	–
γ	Shear rate	100, 200, 300, 400 s^{-1}	[8]
D_{WBC}	Leukocyte diameter	7.5 μm	[49]
ρ_{WBC}	Leukocyte density	1077 kg/m^3	[20]
Y	Leukocyte membrane Young's modulus	300 μN/m	[8]
μ_0	Leukocyte membrane shear stress	76.4 μN/m	–
k_C	Leukocyte membrane bending rigidity	$3aJ$	[39]
η^m	Leukocyte membrane shear viscosity	0.7 μN · s/m	[39,41]
L_{mv}	Microvillus length	0.35 μm	[18]
K^E	Microvillus extensional stiffness	1340 pN/μm (152–1340 pN/μm)	[7,14]
K_{exp}	Experimental microviilus flexural stiffness	7 pN/μm (4–7 pN/μm)	[24–26]
K	Microviilus flexural stiffness	$0.1K_{\text{exp}}$, K_{exp}, $10K_{\text{exp}}$	–
k_f^0	Unstressed forward rate	1 s^{-1}	[50]
k_r^0	Unstressed reverse rate	1 s^{-1}	[50]
σ_b	Bond spring constant	1.0 mN/m	[51]
σ_{ts}	Transition state spring constant	0.98 mN/m	[51]
l_0	Equilibrium bond length	100 nm	[8,11]
K_B	Boltzmann constant	13.8 yJ · K^{-1}	–
T	Absolute temperature	310 K	[8]
	Number of PSGL-1 mol/microvillus	16	[20]
	P-selectin site density	150/μm^2	[10,52]

can be written as

$$\boldsymbol{F}_b = \sigma_b(l - l_0)\hat{\boldsymbol{l}}, \tag{5}$$

where $\hat{\boldsymbol{l}}$ is the unit vector between the positions of the receptor-ligand pair.

The probability P_f of formation of a new bond and the probability P_r of rupture of an existing bond in a time interval Δt are given by

$$P_f = 1 - \exp(-k_{on}\Delta t) \tag{6}$$

and

$$P_r = 1 - \exp(-k_r\Delta t), \tag{7}$$

respectively, where $k_{on} = k_f A_L(n_L - n_b)$, A_L is the local surface area on the ligand-coated substrate accessible to each receptor, and $(n_L - n_b)$ is the density of the unbound ligand. In the time interval Δt, two random numbers P_{rand1} and P_{rand2} between 0 and 1 are generated. A new bond is formed under the condition $P_f > P_{\text{rand1}}$. On the other hand, an existing bond is ruptured when $P_r > P_{\text{rand2}}$. The time interval Δt of 10 μs is used, as suggested in Ref. [20], to simulate leukocyte rolling for a period of 3 s. All parameters used in the AD are presented in Tables I and II.

III. RESULTS AND DISCUSSION

A. Simulation setup

In this study, the leukocyte rolling processes in flows are simulated at different shear rates of $\gamma =$ 100–400 s^{-1}, as shown in Fig. 2. The simulation box is 32 × 46 × 32, where a fluid grid spacing

TABLE II. The simulation dimensionless parameters used in this study.

Parameter	Definition	Value
LBM		
ρ_f	Fluid density	1
ν_f	Fluid kinematic viscosity	0.64
γ	Shear rate	$(1.512, 3.024, 4.536, 6.048) \times 10^{-5}$
(N_x, N_y, N_z)	Simulation box	(32, 48, 32)
$(s_e, s_\epsilon, s_\pi, s_v, s_t, s_q)$	Relaxation rates	(0.41, 0.41, 0.41, 0.41, 1.67, 1.67)
$(\alpha_f, \beta_f, \gamma_f)$	Three free parameters in the MRT	$(3, -5.5, -0.5)$
CGCM		
N_p	Number of solid nodes	714
ρ_{WBC}	Leukocyte density	1.077
Y	Leukocyte membrane Young's modulus	0.0454
μ_0	Leukocyte membrane shear stress	0.0116
k_C	Leukocyte membrane bending rigidity	0.0016
(η^T, η^C)	dissipative parameters	$(1.9896 \times 10^{-4}, 6.6321 \times 10^{-5})$
m	Exponent in power law	6
k_F	FENE coefficient	2.298×10^{-3}
k_A	Global area constant	0.294
k_D	Local area constant	0.00589
k_V	Volume constant	0.294
k_B	Bending coefficient	0.00185
R^C	Cutoff radius of the repulsive potential	0.055
σ_R	Well depth of the repulsive potential	0.05
ϵ_R	Distance where repulsive potential equals zero	2×10^{-5}
LSM		
N_{mv}	Number of microvilli	714
L_{mv}	Microvillus length	0.6571
k_s^{mv}	Microvillus spring constant	0.203
k_a^{mv}	Microviilus angle constant	$(4.58 \times 10^{-5}, 4.58 \times 10^{-4}, 4.58 \times 10^{-3})$
AD		
k_f^0	Unstressed forward rate	1.51287×10^{-7}
k_r^0	Unstressed reverse rate	1.51287×10^{-7}
σ_b	Bond spring constant	0.151495
σ_{ts}	Transition state spring constant	0.14998
l_0	Equilibrium bond length	0.1877
K_BT	Thermal energy	2.2858×10^{-6}
	P-selectin site density	43
Δt	Time interval for adhesion determination	1000
$A_L n_L$	Number of PSGL-1 accessible to each receptor	5

is 5.326×10^{-7} m, and a simulation time step is 1.512×10^{-7} s. A whole leukocyte consists of 714 solid grids for the cell membrane (and also for the microvilli bases), another 714 solid grids for the microvilli tips, and 714 springs for the microvilli. The average membrane particle spacing is 5.326×10^{-7} m, the same as the fluid grid spacing. Two substrates are placed at the bottom and top of the simulation box in the Z direction. The bottom substrate is at rest and coated with P-selectin at a density of $150/\mu\text{m}^{-2}$. A velocity of γH_s is imposed on the top substrate, where H_s is the distance between the two substrates, and γ is the shear rate that varies from 100 to 400 s^{-1}. Periodic boundary conditions are imposed in the X and Y directions. Other simulation parameters are given in Table I. All results in this work, except the behaviors of individual microvilli, are

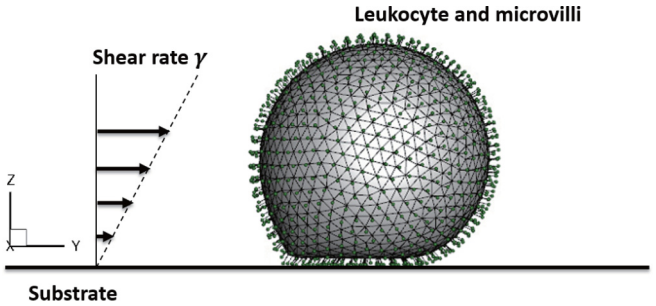

FIG. 2. Simulation configuration.

calculated by a statistical ensemble average of five repeated independent runs. The Reynolds number is $\mathrm{Re} \in [1.172 \times 10^{-3}, 4.688 \times 10^{-3}]$, and therefore the inertial effect can be neglected.

B. Comparison

The resolution test is carried out by using two different sizes of simulation boxes of coarse grids of $32 \times 46 \times 32$ and of fine grids of $48 \times 72 \times 48$ at the same conditions. The time step unit is 2.25 times smaller and the grid length unit is 1.51 times smaller for the fine grids than for the coarse grids. The simulation results are collected and compared in Table III. The average rolling velocity, number of bonds, contact area, and deformation index have similar results and the difference can be ignored, indicating that the coarse grids are satisfactory, and they are used in this work.

A leukocyte rolling on a P-selectin-coated substrate is simulated at a flow shear rate ranging from $\gamma = 100\ \mathrm{s}^{-1}$ to $400\ \mathrm{s}^{-1}$. Here the flexural stiffness of microvilli is set to the experimental value identified by Yao and Shao [24,25]. The simulation results of the average translational velocity of the leukocyte, as a function of shear rate, are compared with those reported by Jadhav *et al.* [8] in Fig. 3(a). Also, the simulation results of the deformation index, defined as leukocyte end-to-end length L divided by leukocyte height H, and the simulation results of the contact area, between the leukocyte and selectin-coated substrate, are compared with those produced by Jadhav *et al.* [8] in Figs. 3(b) and 3(c), respectively. These results agree with the previously published data in this given range of shear rates. The difference can be attributed to distinct numerical models, various simulation constants, and the stochastic nature of the receptor-ligand interaction.

The results include not only the rolling velocity, deformation index, and contact area of leukocytes but also their stop-and-go motion, which is one of the distinctive characteristics of leukocyte rolling. The instantaneous velocity of the leukocyte as a function of time is shown in Fig. 4(a) for the case of the shear rate of $\gamma = 100\ \mathrm{s}^{-1}$ and in Fig. 4(b) for the case of the shear rate of $\gamma = 400\ \mathrm{s}^{-1}$, in which the stop-and-go behavior of the leukocyte rolling is observed. The

TABLE III. The results of the coarse and fine grids are compared at the same condition of $\gamma = 400\ \mathrm{s}^{-1}$.

	Coarse grid	Fine grid
Simulation box	$32 \times 48 \times 32$	$48 \times 72 \times 48$
Grid length unit (μm)	0.536	0.355
Unit time step (s)	1.513×10^{-7}	6.721×10^{-8}
Average rolling velocity (μm/s)	3.01 ± 0.23	2.86 ± 0.25
Number of bonds	348.75 ± 6.18	343.25 ± 20.12
Contact area ($\mu\mathrm{m}^2$)	26.53 ± 0.31	26.24 ± 1.61
Deformation index (L/H)	1.199 ± 0.003	1.194 ± 0.009

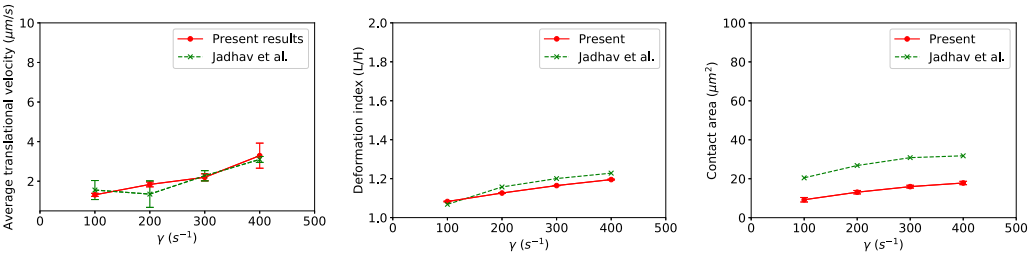

FIG. 3. The comparisons between the present simulation results and those of the previously published data from other groups for (a) the translational velocity, (b) the deformation index (L/H), and (c) the contact area.

comparison between Figs. 4(a) and 4(b) indicates that shorter time pauses and more frequent peaks with increasing shear rate are consistent with the previous finding by Pappu and Bagchi [11].

C. Shear rates on rolling velocity

To study the effects of flexural stiffness of the microvilli of a leukocyte or cell on adhesive dynamics, the flexural stiffness varies at two different levels of K_{exp}, and $10K_{\text{exp}}$, where $K_{\text{exp}} = 7\ \text{pN}/\mu\text{m}$ is taken from the experimental data [24,25], while the extensional stiffness is fixed at $K^E = 1340\ \text{pN}/\mu\text{m}$, which is adopted from Refs. [7,14], for all simulations in this work. In this way, the attention is focused on bending deformation only, not on extension, which has been extensively studied by others [17,19,21]. In this study, the shear rate systematically varies at four different levels: $\gamma = 100\ \text{s}^{-1}$, $200\ \text{s}^{-1}$, $300\ \text{s}^{-1}$, and $400\ \text{s}^{-1}$ at each of the given levels of flexural stiffness.

First, the effects of flexural stiffness of microvilli on the leukocyte rolling velocity at different shear rates are probed. The results of an ensemble average of the translational velocity as a function of shear rate at different levels of flexural stiffness is plotted in Fig. 5(a). It is shown that both the flexural stiffness and shear rate have significant effects on the rolling velocity.

At each of the given levels of flexural stiffness, the rolling velocity increases as the shear rate increases since a larger shear force drives cells to move faster and simultaneously induces a larger number of bonds [see Fig. 5(b)] and an expanded contact area [see Fig. 5(c)]. The bonds and contact area dynamically respond to the external shear force. The results indicate that the slopes of the rolling velocity curves are larger in the large shear rate range than in the small shear rate range,

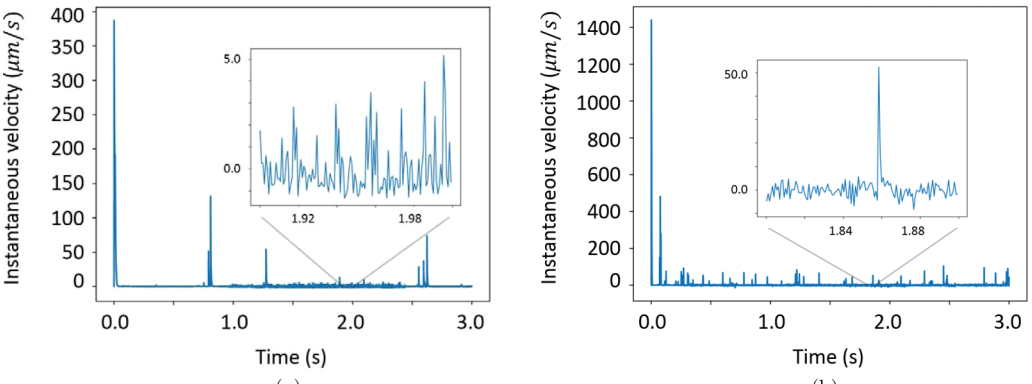

FIG. 4. The instantaneous velocity as a function of time at the shear rates of (a) $100\ \text{s}^{-1}$ and (b) $400\ \text{s}^{-1}$. The magnified drawings represent the instantaneous velocity within a 1-s period.

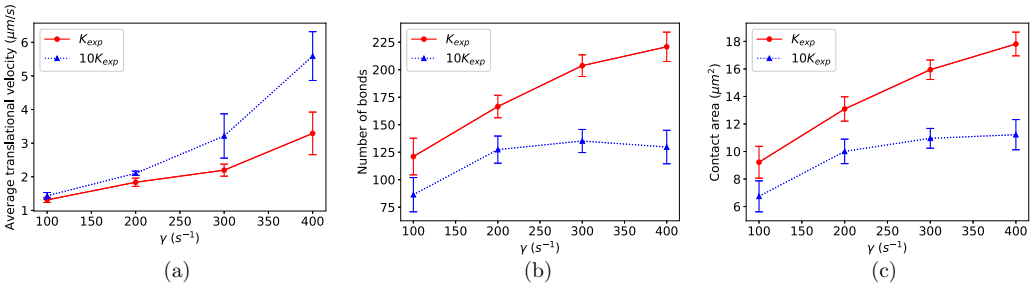

FIG. 5. The simulation results of (a) the average translational velocity, (b) number of bonds, and (c) the contact area as a function of a shear rate at two different levels of the flexural stiffness of microvilli. The shear rate is varied from $\gamma = 100\ \mathrm{s}^{-1}$ to $400\ \mathrm{s}^{-1}$ at each level of flexural stiffness.

revealing that the rolling velocity increases faster in the large shear rate range than in the small shear rate range. On the contrary, the slopes of curves of the number of bonds and the contact areas are smaller in the large shear rate range than in the small shear rate range. As expected, the contact areas and the number of bonds are developed more slowly at the large shear rate range, so that the rolling velocity increases faster.

At a given shear rate, the rolling velocity increases as the flexural stiffness of the microvilli increases or as the flexibility of microvilli decreases, because the microvilli with a larger flexural stiffness have a smaller bending deformation and are likely to be oriented more vertically on the cell surface. Thus, the contact area and number of bonds between the cell and the substrate all become smaller, making the cell roll faster, as compared to cells with more flexible microvilli. The results of the number of bonds and the contact areas are shown in Figs. 5(b) and 5(c), where the number of bonds and the contact areas dramatically decrease as the flexural stiffness increases.

It is observed that the degree of the increase in the rolling velocity due to the flexural stiffness depends on the shear rate. The rolling velocity increases from 3.29 μm/s to 5.59 μm/s at the shear rate of $\gamma = 400\ \mathrm{s}^{-1}$, while the velocity increases from 1.31 μm/s to 1.41 μm/s at the shear rate of $\gamma = 100\ \mathrm{s}^{-1}$. The net increase in rolling velocity due to the flexural stiffness is approximately 20 times larger at $\gamma = 400\ \mathrm{s}^{-1}$ than at $\gamma = 100\ \mathrm{s}^{-1}$, although they have the same levels of flexural stiffness. Therefore, the increase of rolling velocity due to stiffness of microvilli is much more sensitive to a large shear rate than a low shear rate.

Next, the results of the deformation index as a function of the shear rate are given in Fig. 6. The figure shows that at each of the given levels of flexural stiffness, the deformation index increases as the shear rate increases. The deformation index increases by 9%–11% when the shear rate increases from $\gamma = 100\ \mathrm{s}^{-1}$ to $\gamma = 400\ \mathrm{s}^{-1}$. However, at each of the given shear rates, when the flexural stiffness is greatly varied from $K = K_{\mathrm{exp}}$ to $K = 10K_{\mathrm{exp}}$, the deformation index has only 1% variation, illustrating that the cell bulk deformation is more sensitive to the shear rate than the flexural stiffness. In other words, the bulk cell deformation depends strongly on the shear rate and weakly on the flexural stiffness.

For the purpose of visualization, the animations of leukocyte rolling at shear rates of $\gamma = 100\ \mathrm{s}^{-1}$ and $300\ \mathrm{s}^{-1}$ are presented in movie S1 and movie S2 in the Supplemental Material [53].

Subsequently, Fig. 7 illustrates the instantaneous velocity of leukocyte as a function of time at two different levels of the flexural stiffness of microvilli at the shear rate of $\gamma = 300\ \mathrm{s}^{-1}$. In order to characterize translation movement, two types of regimes are defined: rolling and vibrating regimes. When the white blood cell (WBC) instantaneous velocity is larger than 25 μm/s, it is called a rolling regime, and when the instantaneous velocity is between 5 μm/s and 25 μm/s, it is called a vibrating regime. The rolling and vibration regimes correspond to a high peak and low peak period, respectively, in Fig. 7. The average number of the rolling peaks after the first bonding are 44.4 and 103.8 for $K = K_{\mathrm{exp}}$ and $K = 10K_{\mathrm{exp}}$, respectively; the average number of vibrating peaks are 236.8

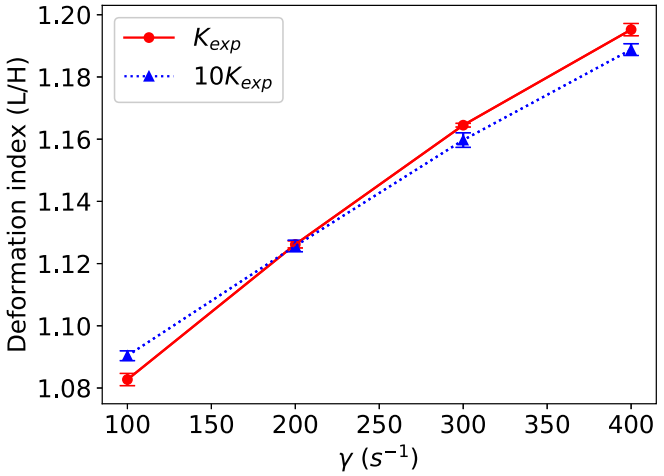

FIG. 6. The simulation results of the deformation index at two different levels of the flexural stiffness of microvilli at the shear rates from 100 s^{-1} to 400 s^{-1}.

and 229.4; and the average pause time, defined by the duration between two rolling peaks, is 0.15 s and 0.08 s. These quantified data show that the WBCs with larger flexural stiffness stay longer in a rolling regime than in a vibrating regime and that the WBCs with the more flexible microvilli have more frequent vibrating fluctuations during the adhesion process. It is suggested that the bending of microvilli shortening the distance between P-selection on the wall and PSGL-1 on microvilli tips results in more bonding and debonding.

D. Shear rate on bond forces

A total adhesive bond force is based on the global coordinates of X, Y, and Z and defined by

$$\boldsymbol{F}^{\text{bond}} = \left\langle \sum_i \boldsymbol{F}_b^i \right\rangle, \tag{8}$$

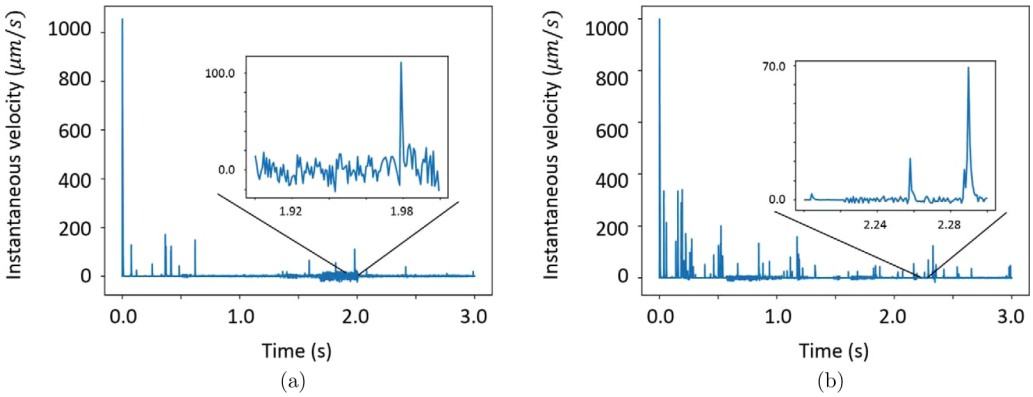

FIG. 7. The instantaneous velocity at microvillus flexural stiffness of (a) K_{exp} and (b)$10K_{\text{exp}}$ at the shear rate of $\gamma = 300$ s^{-1}. The magnified drawing presents the instantaneous velocity in a 0.1-s period.

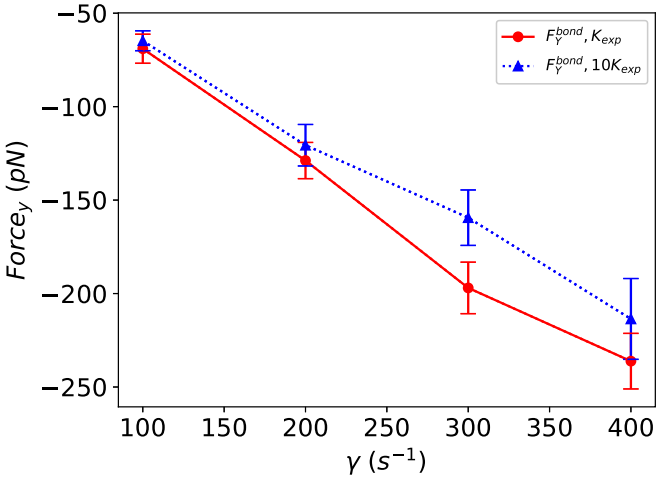

FIG. 8. The simulation results of the Y component of the total adhesive bond force as a function of shear rate at two different levels of flexural stiffness.

where i denotes the ith bond. The Y component of the total adhesive bond force $\boldsymbol{F}_Y^{\text{bond}}$ is in the opposite direction of the fluid flows and resists the cell translation. The results of the Y component as a function of the shear rate at different levels of flexural stiffness are plotted in Fig. 8.

It is shown that the bond forces are strongly influenced not only by shear rates but also by the flexural stiffness of microvilli. At each given level of the flexural stiffness, the Y-component force increases monotonically in the negative direction with the shear rate. This occurs because the adhesive bond force should be balanced by the hydrodynamic shear force, which drives the cell to move; thus a larger shear rate induces a larger responding adhesive bond force. In other words, the bond force strongly depends on the shear rate at each level of the flexural stiffness. At a given shear rate, the cell with the larger flexural stiffness has smaller adhesive forces and should roll faster, as consistently displayed in Fig. 5. The adhesive force increases as the flexural stiffness decreases. The net increase in adhesive forces due to the flexibility of the microvilli is larger in a large shear rate range than in a smaller shear rate range in general, because the larger shear rate may cause more bending deformation of microvilli, which are oriented to be more flattened with the cell surface, allowing a larger contact area and bonding probability. We will come back to the bending deformation in next section. It is clear that an interplay of the roles between the flexural stiffness and flow shear rate determines the final total bond force. The cell motions in the X and Z directions are negligibly small and not interesting, and the force components in the X and Z directions are not needed to be shown in this paper.

E. Bending deformation of microvilli

In order to examine the influence of the flexural stiffness of microvilli on their bending deformation, an angular distribution function $f(\theta)$ of the microvilli is defined by

$$f(\theta) = \frac{1}{\pi n} \sum_i \delta(\theta - \theta_i), \tag{9}$$

where n is the total number of the bonded microvilli, and θ_i is the bending angle of the ith bonded microvillus. The angular distribution function is utilized to describe the probability of finding a microvillus at an angle of θ per unit angle.

The results of an ensemble average of the angular distribution function $\langle f(\theta) \rangle$, as a function of the bending angle at two different levels of the flexural stiffness, are displayed and compared in

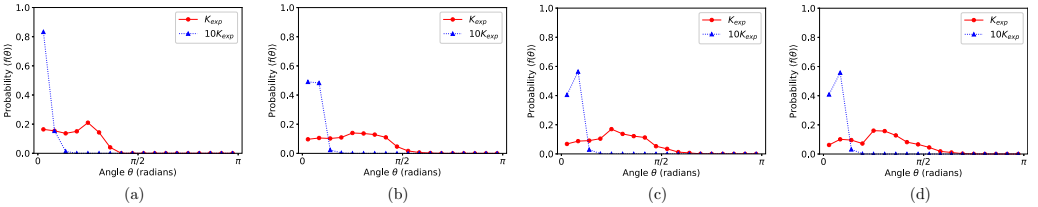

FIG. 9. The simulation results of the angular distribution of the microvilli at two different levels of the microvillus flexural stiffness at shear rates of (a) 100 s^{-1}, (b) 200 s^{-1}, (c) 300 s^{-1}, and (d) 400 s^{-1}.

Fig. 9, at each of the four different shear rates, where red solid and blue dash-dot lines represent the data sets corresponding to $K = K_{\text{exp}}$ and $10K_{\text{exp}}$, respectively. It is shown that the flexural stiffness has an important impact on the bending deformation of microvilli. For example, for the case of the shear rate of $\gamma = 100\ s^{-1}$, two curves of the angular distribution function are compared in Fig. 9(a). One sharp peak appears on the curve of the larger flexural stiffness of $K = 10K_{\text{exp}}$. This peak value is as high as 0.85 and is located near the angle of zero, evidencing that most microvilli are oriented in the direction perpendicular to the cell surface or along the angular baseline. As the flexural stiffness reduces to a lower level of $K = K_{\text{exp}}$, two peaks are observed: one peak with a value of 0.16 is located at $0 < \theta < 1/9\pi$, and the other with a value of 0.21 is located at $4/9\pi < \theta < 5/9\pi$, indicating that as the flexural stiffness decreases, the bending angle increases, and the microvilli tend to be flattened on the cell surface. A similar behavior is observed at every given shear rate. It is pointed out that for a given flexural stiffness, the peak becomes lower and wider and shifts to the side of the angle of $\theta = \pi/2$ as the shear rate increases, suggesting that more microvilli are moved from the angular baseline direction to their perpendicular direction.

F. Bending behavior of individual microvillus

To closely monitor the process of bonding formation at the microscopic scale of a single microvillus during cell rolling, two individual microvilli are selected, and their bending angles as a function of time are recorded as a sample. Figure 10 depicts the angles of the two individual microvilli as a function of time, where the yellow solid lines and blue dotted lines represent the duration involved in bonded and nonbonded states, respectively. Each figure also includes both the side and bottom views of the leukocyte. For the bottom view, the red marker specifies the

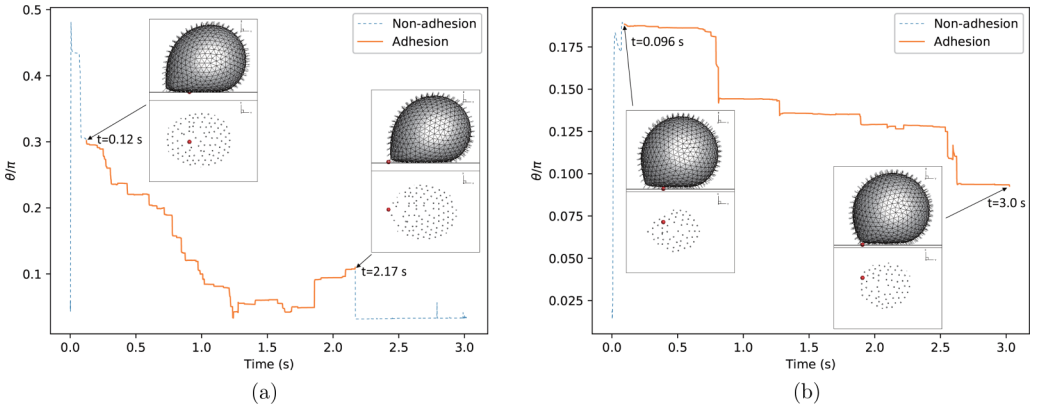

FIG. 10. The bending angle as a function of time for (a) the single microvillus initially located near the center of the contact area at $\gamma = 400\ s^{-1}$ and (b) the single microvillus initially located near the center of the contact area at $\gamma = 100\ s^{-1}$. The stiffness of the microvillus is fixed at the experimental value.

particularly selected single microvillus (e.g., microvilli no. 1 and 2), and the black points denote the other microvilli. Microvillus no. 1 is initially located near the center of the contact area, while no. 2 is initially located near the right edge of the contact area. The shear rate $\gamma = 400\ \mathrm{s}^{-1}$ is applied on microvilli no. 1, and the shear rate $\gamma = 100\ \mathrm{s}^{-1}$ is imposed on no. 2.

The variation of the bending angle of microvillus no. 1 is shown in Fig. 10(a) as the microvillus moves from the center to the left edge of the contact area during the rolling process. In the initial period ($t < 0.12$ s), there is nonbonding involved (blue dotted line). The microvillus stands vertically on the cell surface with a very small bending angle and then is quickly bent with a large angle and flattened with the surface. Soon after that, a receptor-ligand bond is developed and formed at $t = 0.12$ s. As the leukocyte continues to roll, the angle of the microvillus first decreases and then increases. Finally, the bond is broken at $t = 2.17$ s, and the microvillus becomes vertical again with a small bending angle when the microvillus moves to the left edge of the contact area. This nonbonding, bonding, and debonding process corresponds to the stop-and-go motion. The bending behavior of microvillus no. 2, moving to the edge of the contact area during the rolling process, is shown in Fig. 10(b). A bond is formed on the vertical microvillus at $t = 1.31$ s. Unlike no. 1, the bending angle decreases monotonically, and this microvillus becomes more vertical with the cell surface when it migrates to the center of the contact area. The major difference is that the bending angles of no. 2 are smaller most time, as expected, due to the smaller shear rate $\gamma = 100\ \mathrm{s}^{-1}$. The rupture of bonding is observed in microvillus no. 1 only. Finally, for visualization purpose, two movies are available in the Supplemental Material [53].

IV. CONCLUSIONS

The details of the LLM, including LBM, IBM, CGCM, and AD, are presented in this paper. This method can treat not only extensional and compressional but also bending deformation of microvilli of a leukocyte or cell in flows. In order to study the effects of shear rates on bending deformation of microvilli of leukocytes, in the simulations the shear rate is varied at four different levels and the flexural stiffness of the microvilli is varied at different levels for each given level of the shear rate. The cell rolling velocity, adhesive bond force, number of bonds, contact area, bending angular distribution, and cell deformation index are computed. An angular distribution function is used to analyze the bending deformation of microvilli.

Several interesting behaviors are revealed from simulations:

(1) At each of the given levels of the flexural stiffness of microvilli, their bending angles, total adhesive bond force, number of bonds, contact area, deformation index, and cell rolling velocity increase as the shear rate increases since a larger external shear hydrodynamic force drives cells to move faster and simultaneously induces a larger adhesive force.

(2) At each given shear rate, the bending angles of microvilli increase as their flexural stiffness decreases, and the microvilli become more flattened on cell surface. Therefore, the contact area, number of bonds, and adhesive force increase, resulting in a decrease in rolling velocity. The degree of the decrease in rolling velocity depends on both the shear rate and flexural stiffness. The net decrease in the rolling velocity due to flexibility of the microvilli is larger in in a large shear rate range than in the smaller shear rate range. It is clear that the interplay of roles between shear rate and flexural stiffness determines final adhesive bond force and rolling velocity.

(3) The bulk cell deformation depends strongly on the shear rate and weakly on the flexural stiffness of microvilli.

(4) The bonding and debonding process as a function of instant time is observed for individual microvillus in term of bending angle.

The above information may enhance understanding of effects of shear rate on adhesion of WBCs.

ACKNOWLEDGMENTS

T.-H.W. and D.Q. thank Dr. M. Di Pierro and Yi-Chin Huang for proofreading and writing advice. T.-H.W. also acknowledges the Gwen Frostic Doctoral Fellowship for partially supporting this work,

and D.Q. acknowledges the award of the Faculty Creativity Initiative of the College of Engineering and Applied Sciences at Western Michigan University.

APPENDIX

1. Lattice-Boltzmann method

The motion of Newtonian fluid is governed by the continuity and Navier-Stokes equations as

$$\nabla \cdot \mathbf{u} = 0, \tag{A1}$$

$$\rho_f \left[\frac{\partial \mathbf{u}}{\partial t} + (\mathbf{u} \cdot \nabla \mathbf{u}) \right] = -\nabla p + \mu \nabla^2 \mathbf{u} + \mathscr{F}, \tag{A2}$$

where $\mathbf{u}$ is the fluid velocity, ρ_f the fluid density, p the pressure, μ the fluid dynamic viscosity, and $\mathscr{F}$ the force source term. In this study, the partial differential equations [Eqs. (A1) and (A2)] are not solved directly. Instead, the LBM is used to obtain fluid flow behavior. Previous work has demonstrated that the solution of the LBM is equivalent to that of the Navier-Stokes equations when the Mach number is smaller than 0.3 [30]. Importantly, the kinetic nature of the LBM makes it more suitable for simulating the multicomponent flows such as blood [54–58]. More features of the LBM can be found in previous studies [35].

The multiple-relaxation-time (MRT) lattice Boltzmann equation [59] in a D3Q19 lattice model with a forcing term is used and expressed as

$$\boldsymbol{f}(\mathbf{x} + \mathbf{e}_i \delta t, t + \delta t) - \boldsymbol{f}(\mathbf{x}, t) = -\mathbf{M}^{-1}\mathbf{S}[\mathbf{m}(\mathbf{x}, t) - \mathbf{m}^{eq}(\mathbf{x}, t)] + \delta t \mathbf{M}^{-1}\widehat{\boldsymbol{F}}, \tag{A3}$$

where $\boldsymbol{f}(\mathbf{x}, t)$ and $\mathbf{m}(\mathbf{x}, t)$ are the fluid distribution functions at position $\mathbf{x}$ and time t in the velocity and moment spaces, respectively; $\mathbf{m}^{eq}$ denotes the equilibrium distribution function in moment space; δt represents the time interval; $\mathbf{e}_i$ is the discrete velocity set where $i \in \{0, 1, 2, \ldots, 18\}$ are the discrete directions; $\mathbf{S}$ is the diagonal collision matrix; $\mathbf{M}$ is the transformation matrix (given in the Appendix of Ref. [59]) which transfers the distribution functions from the velocity space into the moment space; and $\widehat{\boldsymbol{F}}$ is the moment of the forcing term in the moment space.

In the D3Q19 model, the discrete velocity set $\mathbf{e}_i$ is written as

$$\mathbf{e}_i = \begin{cases} (0, 0, 0) & i = 0 \\ (\pm 1, 0, 0), (0, \pm 1, 0), (0, 0, \pm 1) & i = 1\text{–}6 \\ (\pm 1, \pm 1, 0), (\pm 1, 0, \pm 1), (0, \pm 1, \pm 1) & i = 7\text{–}18 \end{cases}, \tag{A4}$$

and the diagonal collision matrix $\mathbf{S}$ is written as

$$\mathbf{S} = (0, s_e, s_\epsilon, 0, s_q, 0, s_q, 0, s_q, s_\nu, s_\pi, s_\nu, s_\pi, s_\nu, s_\nu, s_\nu, s_t, s_t, s_t), \tag{A5}$$

while shear and bulk viscosities are given by

$$\nu = \frac{1}{3}\left(\frac{1}{s_\nu} - \frac{1}{2}\right)\delta t, \tag{A6}$$

$$\zeta = \frac{2}{9}\left(\frac{1}{s_e} - \frac{1}{2}\right)\delta t, \tag{A7}$$

where s_ν is related to the shear viscosity. As suggested by Pan *et al.* [60], the other relaxation rates are set as $s_e = s_\epsilon = s_\pi = s_\nu$ and $s_t = s_q = 8 \cdot \frac{2 - s_\nu}{8 - s_\nu}$.

The distribution functions in the moment space $\mathbf{m}$ and the corresponding equilibria $\mathbf{m}^{eq}$ are written by

$$\mathbf{m} = (\rho_f, e_f, \epsilon_f, j_x, q_x, j_y, q_y, j_z, q_z, 3p_{xx}, 3\pi_{xx}, p_{ww}, \pi_{ww}, p_{xy}, p_{yz}, p_{zx}, t_x, t_y, t_z)^T, \tag{A8}$$

$$\mathbf{m}^{eq} = \rho_f(1, -11 + 19u^2, \alpha_f + \beta_f u^2, u_x, -\frac{2}{3}u_x, u_y, -\frac{2}{3}u_y, u_z, -\frac{2}{3}u_z, 3u_x^2 - u^2, \frac{\gamma_f p_{xx}^{eq}}{\rho}, u_y^2 - u_z^2, \frac{\gamma_f p_{ww}^{eq}}{\rho}, u_x u_y, u_y u_z, u_z u_x, 0, 0, 0)^T, \tag{A9}$$

where e_f and ϵ_f represent energy and energy squared, $j_{x,y,z}$ are components of the momentum, $q_{x,y,z}$ are components of the heat flux, $p_{xy,yz,zx}$ are the symmetric and traceless strain-rate tensor, $\pi_{xx,ww}$ are the fourth-order moments and $t_{x,y,z}$ are the third-order moments [59], $u^2 = u_x^2 + u_y^2 + u_z^2$ denotes the fluid velocity squared, and the three parameters $\alpha_f = 3$, $\beta_f = \frac{-11}{2}$, and $\gamma_f = \frac{-1}{2}$ are chosen.

Furthermore, according to the work by Guo *et al.* [61,62], the moment of the forcing term in the moment space $\widehat{\boldsymbol{F}}$ can be written as

$$\widehat{\boldsymbol{F}} = \left(\mathbf{I} - \tfrac{1}{2}\mathbf{S}\right)\mathbf{M}\overline{\boldsymbol{F}}, \tag{A10}$$

where $\mathbf{I}$ is the unity matrix, $\overline{\boldsymbol{F}} = (\overline{F}_0, \overline{F}_1, \ldots, , \overline{F}_{18})^T$, and

$$\overline{F}_i = \omega_i \left[\frac{\mathbf{e}_i \cdot \boldsymbol{F}}{c_s^2} + \frac{\mathbf{u}\boldsymbol{F} : \left(\mathbf{e}_i\mathbf{e}_i - c_s^2\mathbf{I}\right)}{c_s^4} \right], \tag{A11}$$

where $\boldsymbol{F}$ is the body force, $c_s = \sqrt{\frac{1}{3}}$ is the sound speed, and ω_i is the weight associated with the lattice model and defined by

$$\omega_i = \begin{cases} \frac{1}{3} & i = 0 \\ \frac{1}{18} & i = 1 - 6 \\ \frac{1}{36} & i = 7 - 18 \end{cases}. \tag{A12}$$

The fluid velocity $\mathbf{u}$ is given by

$$\rho_f \mathbf{u} = \sum_i f_i \mathbf{e}_i + \frac{1}{2}\delta t \boldsymbol{F}. \tag{A13}$$

All parameters used in the LBM are given in Tables I and II.

2. Immersed boundary method

In the LBM, the fluid particles are in regular Eulerian grids, whereas the solid particles are in Lagrangian grids. Therefore, a solid grid may not coincide with its adjacent fluid grids. The IBM is used to achieve nonslip boundary condition in the fluid-solid interfaces. For the purpose, a discrete Dirac delta function δ^D is taken to interpolate the fluid velocity at the position of a solid boundary grid from its surrounding fluid grids. The discrete Dirac delta function [43] is written as

$$\delta^D(\Delta\mathbf{r}) = \begin{cases} \frac{1}{64h^3}\left(1 + \cos\frac{\pi\Delta x}{2h}\right)\left(1 + \cos\frac{\pi\Delta y}{2h}\right)\left(1 + \cos\frac{\pi\Delta z}{2h}\right) & |\Delta\mathbf{r}| \leqslant 2h \\ 0 & |\Delta\mathbf{r}| > 2h \end{cases}, \tag{A14}$$

where h is the fluid grid spacing and $\Delta\mathbf{r} = (\Delta x, \Delta y, \Delta z)$ is the distance between the positions of the solid boundary grid and its surrounding fluid grids.

To present the IBM, the solid boundary domain Γ and fluid boundary domain Π are defined. The solid boundary domain Γ is constituted by all the solid grids on the surface, and the fluid boundary domain Π is defined as a spherical volume of a radius of $2h$ centered at a solid boundary grid position $\mathbf{r}^b$. The unforced fluid velocity $\mathbf{u}^*$ at $\mathbf{r}^b$ is represented by

$$\mathbf{u}^*(\mathbf{r}^b, t) = \int_\Pi \mathbf{u}^*(\mathbf{r}, t)\delta^D(\mathbf{r} - \mathbf{r}^b)d\mathbf{r}, \tag{A15}$$

where $\mathbf{r}$ is a variable and goes all the positions of the fluid grids in the fluid domain Π during the integration. Due to the no-slip boundary condition, the forced fluid velocity $\mathbf{u}(\mathbf{r}^b, t)$ should be equal to the solid velocity $\mathbf{U}^b(\mathbf{r}^b, t)$ as

$$\mathbf{u}(\mathbf{r}^b, t) = \mathbf{u}^*(\mathbf{r}^b, t) + \delta t \frac{\mathcal{F}(\mathbf{r}^b, t)}{\rho_f} = \mathbf{U}^b(\mathbf{r}^b, t), \tag{A16}$$

where $\mathcal{F}$ is the fluid-solid interaction force exerted on the fluid. Therefore, the interaction force $\mathcal{F}$ exerted on the fluid at the solid boundary position can be expressed by

$$\mathcal{F}(\mathbf{r}^b, t) = \frac{\rho_f[\mathbf{U}^b(\mathbf{r}^b, t) - \mathbf{u}^*(\mathbf{r}^b, t)]}{\delta t}. \tag{A17}$$

Thus, the interaction force acting on the solid grids by the surrounding fluid is given by

$$\boldsymbol{F}^H(\mathbf{r}^b, t) = -\mathcal{F}(\mathbf{r}^b, t). \tag{A18}$$

The discrete Dirac delta function is utilized again to distribute the interaction force $\mathcal{F}(\mathbf{r}^b, t)$ to the surrounding fluid grids by

$$\boldsymbol{F}(\mathbf{r}, t) = \int_\Gamma \mathcal{F}(\mathbf{r}^b, t)\delta^D(\mathbf{r} - \mathbf{r}^b)\, d\mathbf{r}^b, \tag{A19}$$

where $\boldsymbol{F}(\mathbf{r}, t)$ is the distributed body force and can be used in Eq. (A11).

3. Coarse-grained cell model

A leukocyte can be simulated by a coarse-grained cell model (CGCM), presented by Fedosov *et al.* [38], in which the leukocyte is assumed to be a spherical membrane. The membrane is considered as a two-dimensional triangulated network. An open source MATLAB mesh generator presented by Persson *et al.* [63] was used in this study for creating meshes.

In the triangulated network, N_p denotes the number of solid grids, N_b the number of edges, and N_e the number of triangles. Four types of potential energies are calculated between solid grids. The total potential energy of the membrane can be written as

$$U^{\text{total}} = U^{\text{in-plane}} + U^{\text{area}} + U^{\text{volume}} + U^{\text{bending}}. \tag{A20}$$

The in-plane potential energy term $U^{\text{in-plane}}$ has several formulas constituted by two-body and three-body energies. In this study, an edge is considered as a nonlinear spring, whose energy is constituted by the combination of the finitely extensible nonlinear elastic (FENE) and power-law (PL) potential energies, as

$$U^{\text{in-plane}} = \sum_j^{N_b} -\frac{1}{2}k_F R_0^2 \ln\left[1 - \left(\frac{r}{R_0}\right)^2\right] + \frac{k_P}{(m-1)r^{m-1}} \quad m > 0 \text{ and } m \neq 1, \tag{A21}$$

where k_F is a constant coefficient of the FENE potential, R_0 and r are the maximum and instant distances between two solid grids, respectively, k_P is the coefficient of the PL potential energy, and m is the exponent of the power law. Apparently, $U^{\text{in-plane}}$ is only a two-body energy of a nonlinear spring.

The area conservation and volume conservation energies, U^{area} and U^{volume}, are the three-body energies, which exist in a triangle constituted by three neighboring solid grids. The area and volume

conservation energies are defined as

$$U^{\text{area}} = \frac{k_A\left(A - A_0^{\text{tot}}\right)^2}{2A_0^{\text{tot}}} + \sum_j^{N_e} \frac{k_D\left(A_j - A_j^0\right)^2}{2A_j^0}, \tag{A22}$$

$$U^{\text{volume}} = \frac{k_V\left(V - V_0^{\text{tot}}\right)^2}{2V_0^{\text{tot}}}, \tag{A23}$$

where k_A, k_D, and k_V are the global area, local area, and volume constraint constants, respectively. The term A and V represent the instantaneous entire area and volume, respectively, while A_0^{tot} and V_0^{tot} are the initial total area and volume and A_j^0 and A_j are the initial and instantaneous local area of the jth triangle.

Furthermore, the bending energy U^{bending} exists between two adjacent triangles (four adjacent solid grids) and is given by

$$U^{\text{bending}} = \sum_j^{N_b} k_B[1 - \cos(\theta_j - \theta_0)], \tag{A24}$$

where k_B is the bending coefficient and θ_j and θ_0 are the instantaneous and initial angles, respectively, between two adjacent triangles which have the common edge j.

The total elastic force $\boldsymbol{F}_i^E$ exerted on the ith grid in the CGCM is computed by

$$\boldsymbol{F}_i^E = -\boldsymbol{\nabla}_i(U^{\text{in-plane}} + U^{\text{area}} + U^{\text{volume}} + U^{\text{bending}}). \tag{A25}$$

The gradient is calculated analytically, and the answers are used in the code.

The CGCM [13,38–41] also addresses the membrane viscosity by adding the dissipative $\boldsymbol{F}_{ij}^D$ for each spring (edge) as

$$\boldsymbol{F}_{ij}^D = -\eta^T \mathbf{v}_{ij} - \eta^C(\mathbf{v}_{ij} \cdot \mathbf{e}_{ij})\mathbf{e}_{ij}, \tag{A26}$$

where η^T and η^C are dissipative coefficients, respectively; and $\mathbf{v}_{ij}$ and $\mathbf{e}_{ij}$ are the relative velocity and unit vector, respectively, between the ith and jth grids. The membrane shear viscosity η^m is related to the dissipative parameters (η^T and η^C), as follows:

$$\eta^m = \sqrt{3}\eta^T + \frac{\sqrt{3}}{4}\eta^C, \tag{A27}$$

$$\eta^C = \frac{\eta^T}{3}. \tag{A28}$$

A repulsive force is added on leukocytes between the leukocytes and substrate in the Z direction (perpendicular to the substrate) when the leukocytes are close to the substrate. The repulsive force is borrowed from the gradient of the Lennard-Jones potential (U^{LJ}) with a negative sign, as

$$\boldsymbol{F}^R(\delta z) = \begin{cases} -\boldsymbol{\nabla}_z\{U^{LJ}(\delta z)\} = -\boldsymbol{\nabla}_z\left\{4\epsilon_R\left[\left(\frac{\sigma_R}{\delta z}\right)^{12} - \left(\frac{\sigma_R}{\delta z}\right)^6\right]\right\} & \delta z \leqslant R^C \\ 0 & \delta z > R^C \end{cases}, \tag{A29}$$

where δz is the distance above the substrate, R^C is the cutoff radius, ϵ_R is the well depth of the potential, and σ_R is the distance between the substrate surface and the position where $U^{LJ} = 0$. Therefore, the total force exerted on the ith solid grid is given by

$$\boldsymbol{F}_i^T = \boldsymbol{F}_i^E + \sum_j \boldsymbol{F}_{ij}^D + \boldsymbol{F}_i^H + \boldsymbol{F}_i^R, \tag{A30}$$

where $\boldsymbol{F}^T$, $\boldsymbol{F}^E$, $\boldsymbol{F}^D$, $\boldsymbol{F}^H$, and $\boldsymbol{F}^R$ denote the total, elastic, dissipative, hydrodynamic, and repulsive forces, respectively; and j denotes the grid nearby the ith solid grid. Once the total force of a solid

grid is obtained, the leap-frog algorithm is used to obtain the position and velocity of each solid grid during the simulation run.

Next, six parameters (k_F, k_P, k_A, k_D, k_V, and k_B) must be determined in the CGCM. First, the potential coefficient of power law k_P can be described in terms of k_F since the attractive term should be equal to the repulsive term at the equilibrium point in $U^{\text{in-plane}}$. By setting the exponent of the power law $m = 6$ and $R_0 = 1.75r$, the potential coefficient of power law k_P can be written by

$$k_P \cong 1.4848 k_F r^{m+1} = 1.4848 k_F r^7. \tag{A31}$$

Second, according to Fedosov *et al.* [38,39], the shear stress μ_0 based on the $U^{\text{in-plane}}$ is given by

$$\mu_0 = \frac{\sqrt{3}}{4}\left\{\frac{2k_F\left(\frac{r}{R_0}\right)^2}{\left[1-\left(\frac{r}{R_0}\right)^2\right]^2} + \frac{k_P(m+1)}{r^{m+1}}\right\}, \tag{A32}$$

and the compression modulus κ of cell is given by

$$\kappa = 2\mu_0 + k_A + k_D. \tag{A33}$$

The linear Young's modulus Y and Poisson's ratio ν^p of the cell are expressed by

$$Y = \frac{4\kappa\mu_0}{\kappa + \mu_0}, \tag{A34}$$

$$\nu^p = \frac{\kappa - \mu_0}{\kappa + \mu_0}. \tag{A35}$$

To achieve incompressibility and to make $k_A + k_D \gg \mu_0$, Fedosov *et al.* showed that a nearly incompressible membrane is achieved when $k_A + k_D = 500\mu_0$. That assumption is followed. In addition, the bending coefficient k_B in the CGCM is given by

$$k_B = \frac{2}{\sqrt{3}} k_C, \tag{A36}$$

where k_C is the bending rigidity. All parameters used in the CGCM are collected in Tables I and II.

[1] J. N. Kochenderfer, W. H. Wilson, J. E. Janik, M. E. Dudley, M. Stetler-Stevenson, S. A. Feldman, I. Maric, M. Raffeld, D.-A. N. Nathan, B. J. Lanier, R. A. Morgan, and S. A. Rosenberg, Eradication of b-lineage cells and regression of lymphoma in a patient treated with autologous T cells genetically engineered to recognize CD19, Blood **116**, 4099 (2010).

[2] H. J. Jackson, S. Rafiq, and R. J. Brentjens, Driving CAR T-cells forward, Nat. Rev. Clin. Oncol. **13**, 370 (2016).

[3] D. A. Hammer and S. M. Apte, Simulation of cell rolling and adhesion on surfaces in shear flow: General results and analysis of selectin-mediated neutrophil adhesion, Biophys. J. **63**, 35 (1992).

[4] K.-C. Chang, D. F. J. Tees, and D. A. Hammer, The state diagram for cell adhesion under flow: Leukocyte rolling and firm adhesion, Proc. Natl. Acad. Sci. USA **97**, 11262 (2000).

[5] S. K. Bhatia, M. R. King, and D. A. Hammer, The state diagram for cell adhesion mediated by two receptors, Biophys. J. **84**, 2671 (2003).

[6] D. B. Khismatullin and G. A. Truskey, A 3D numerical study of the effect of channel height on leukocyte deformation and adhesion in parallel-plate flow chambers, Microvasc. Res. **68**, 188 (2004).

[7] D. B. Khismatullin and G. A. Truskey, Three-dimensional numerical simulation of receptor-mediated leukocyte adhesion to surfaces: Effects of cell deformability and viscoelasticity, Phys. Fluids **17**, 031505 (2005).

[8] S. Jadhav, C. D. Eggleton, and K. Konstantopoulos, A 3-D computational model predicts that cell deformation affects selectin-mediated leukocyte rolling, Biophys. J. **88**, 96 (2005).
[9] E. Y. H. Park, McRae J. Smith, E. S. Stropp, K. R. Snapp, J. A. DiVietro, W. F. Walker, D. W. Schmidtke, S. L. Diamond, and M. B. Lawrence, Comparison of PSGL-1 microbead and neutrophil rolling: Microvillus elongation stabilizes P-selectin bond clusters, Biophys. J. **82**, 1835 (2002).
[10] T. Yago, A. Leppänen, H. Qiu, W. D. Marcus, M. U. Nollert, C. Zhu, R. D. Cummings, and R. P. McEver, Distinct molecular and cellular contributions to stabilizing selectin-mediated rolling under flow, J. Cell Biol. **158**, 787 (2002).
[11] V. Pappu and P. Bagchi, 3D computational modeling and simulation of leukocyte rolling adhesion and deformation, Comput. Biol. Med. **38**, 738 (2008).
[12] V. Pappu, S. K. Doddi, and P. Bagchi, A computational study of leukocyte adhesion and its effect on flow pattern in microvessels, J. Theor. Biol. **254**, 483 (2008).
[13] D. A. Fedosov, B. Caswell, and G. Em Karniadakis, Wall shear stress-based model for adhesive dynamics of red blood cells in malaria, Biophys. J. **100**, 2084 (2011).
[14] Z. Y. Luo, S. Qi Wang, L. He, T. J. Lu, F. Xu, and B. F. Bai, Front tracking simulation of cell detachment dynamic mechanism in microfluidics, Chem. Eng. Sci. **97**, 394 (2013).
[15] Z. Y. Luo and B. F. Bai, State diagram for adhesion dynamics of deformable capsules under shear flow, Soft Matter **12**, 6918 (2016).
[16] L. L. Xiao, Y. Liu, S. Chen, and B. M. Fu, Effects of flowing RBCs on adhesion of a circulating tumor cell in microvessels, Biomech. Model. Mechanobiol. **16**, 597 (2017).
[17] K. E. Caputo and D. A. Hammer, Effect of microvillus deformability on leukocyte adhesion explored using adhesive dynamics simulations, Biophys. J. **89**, 187 (2005).
[18] J.-Y. Shao, H. P. Ting-Beall, and R. M. Hochmuth, Static and dynamic lengths of neutrophil microvilli, Proc. Natl. Acad. Sci. USA **95**, 6797 (1998).
[19] P. Pawar, S. Jadhav, C. D. Eggleton, and K. Konstantopoulos, Roles of cell and microvillus deformation and receptor-ligand binding kinetics in cell rolling, Am. J. Physiol. Heart Circ. Physiol. **295**, H1439 (2008).
[20] M. K. Pzalska, A. Zarbock, J. E. Pickard, and K. Ley, Event-tracking model of adhesion identifies load-bearing bonds in rolling leukocytes, Microcirculation **16**, 781 (2009).
[21] M. K. Pospieszalska and K. Ley, Dynamics of microvillus extension and tether formation in rolling leukocytes, Cell. Mol. Bioeng. **2**, 207 (2009).
[22] J.-Y. Shao, Biomechanics of leukocyte and endothelial cell surface, in *Current Topics in Membranes*, edited by Klaus Ley, Current Topics in Membranes Vol. 64 (Academic Press, 2009), pp. 25–45.
[23] L. L. Munn, R. J. Melder, and R. K. Jain, Role of erythrocytes in leukocyte-endothelial interactions: Mathematical model and experimental validation, Biophys. J. **71**, 466 (1996).
[24] D.-K. Yao and J.-Y. Shao, Flexibility of single microvilli on live neutrophils and lymphocytes, Phys. Rev. E **76**, 021907 (2007).
[25] D.-K. Yao and J.-Y. Shao, A novel technique of quantifying flexural stiffness of rod-like structures, Cell. Mol. Bioeng. **1**, 75 (2008).
[26] S. I. Simon, T. Nyunt, K. Florine-Casteel, K. Ritchie, H. P. Ting-Beall, E. Evans, and D. Needham, Dynamics of neutrophil membrane compliance and microstructure probed with a micropipet-based piconewton force transducer, Ann. Biomed. Eng. **35**, 595 (2007).
[27] T.-H. Wu and D. Qi, Role of flexural stiffness of leukocyte microvilli in adhesion dynamics, Phys. Rev. Fluids **3**, 031101 (2018).
[28] D. Qi, Lattice Boltzmann simulations of particles in non-zero Reynolds number flows, J. Fluid Mech. **385**, 41 (1999).
[29] P. Lallemand and L.-S. Luo, Theory of the lattice Boltzmann method: Dispersion, dissipation, isotropy, Galilean invariance, and stability, Phys. Rev. E **61**, 6546 (2000).
[30] S. Succi, *The Lattice Boltzmann Equation: For Fluid Dynamics and Beyond* (Oxford University Press, Oxford, 2001).
[31] D. Qi and L.-S. Luo, Rotational and orientational behavior of three-dimensional spheroidal particles in Couette flows, J. Fluid Mech. **477**, 201 (2003).

[32] D. Qi, Direct simulations of flexible cylindrical fiber suspensions in finite Reynolds number flows, J. Chem. Phys. **125**, 114901 (2006).
[33] D. Qi, Y. Liu, W. Shyy, and H. Aono, Simulations of dynamics of plunge and pitch of a three-dimensional flexible wing in a low Reynolds number flow, Phys. Fluids **22**, 091901 (2010).
[34] C. K. Aidun and J. R. Clausen, Lattice-Boltzmann method for complex flows, Annu. Rev. Fluid Mech. **42**, 439 (2010).
[35] Z. Guo and C. Shu, *Lattice Boltzmann Method and Its Applications in Engineering*, Vol. 3 (World Scientific, Singapore, 2013).
[36] D. Qi, G. He, and Y. Liu, Lattice Boltzmann simulations of a pitch-up and pitch-down maneuver of a chord-wise flexible wing in a free stream flow, Phys. Fluids **26**, 021902 (2014).
[37] D. Qi and R. Gordnier, Effects of deformation on lift and power efficiency in a hovering motion of a chord-wise flexible wing, J. Fluids Struct. **54**, 142 (2015).
[38] D. A. Fedosov, B. Caswell, and G. Em Karniadakis, A multiscale red blood cell model with accurate mechanics, rheology, and dynamics, Biophys. J. **98**, 2215 (2010).
[39] D. A. Fedosov, Multiscale modeling of blood flow and soft matter, Ph.D. thesis, Brown University, 2010.
[40] D. A. Fedosov, J. Fornleitner, and G. Gompper, Margination of White Blood Cells in Microcapillary Flow, Phys. Rev. Lett. **108**, 028104 (2012).
[41] D. A. Fedosov and G. Gompper, White blood cell margination in microcirculation, Soft Matter **10**, 2961 (2014).
[42] T.-H. Wu, R.-S. Guo, G.-W. He, Y.-M. Liu, and D. Qi, Simulation of swimming of a flexible filament using the generalized lattice-spring lattice-Boltzmann method, J. Theor. Biol. **349**, 1 (2014).
[43] C. S. Peskin, The immersed boundary method, Acta Numerica **11**, 479 (2002).
[44] T.-H. Wu and D. Qi, Lattice-Boltzmann lattice-spring simulations of influence of deformable blockages on blood fluids in an elastic vessel, Comput. Fluids **155**, 103 (2017).
[45] Ye Luo, T.-H. Wu, and D. Qi, Lattice-Boltzmann lattice-spring simulations of flexibility and inertial effects on deformation and cruising reversal of self-propelled flexible swimming bodies, Comput. Fluids **155**, 89 (2017).
[46] Y. Tang, T.-H. Wu, G.-W. He, and D. Qi, Multi-flexible fiber flows: A direct-forcing immersed boundary lattice-Boltzmann lattice-spring approach, Int. J. Multiphase Flow **99**, 408 (2018).
[47] M. Dembo, D. C. Torney, K. Saxman, and D. Hammer, The reaction-limited kinetics of membrane-to-surface adhesion and detachment, Proc. R. Soc. London B **234**, 55 (1988).
[48] R. Skalak and S. Chien, *Handbook of Bioengineering* (McGraw-Hill, New York, 1987).
[49] P. Tandon and S. L. Diamond, Kinetics of β_2-integrin and L-selectin bonding during neutrophil aggregation in shear flow, Biophys. J. **75**, 3163 (1998).
[50] P. Mehta, R. D. Cummings, and R. P. McEver, Affinity and kinetic analysis of P-selectin binding to P-selectin glycoprotein ligand-1, J. Biol. Chem. **273**, 32506 (1998).
[51] M. Dembo, On peeling an adherent cell from a surface, in *Lectures on Mathematics in the Life Sciences*, Vol. 24 (American Mathematical Society, Providence, 1994), pp. 51–77.
[52] K. L. Moore, K. D. Patel, R. E. Bruehl, F. Li, D. A. Johnson, H. S. Lichenstein, R. D. Cummings, D. F. Bainton, and R. P. McEver, P-selectin glycoprotein ligand-1 mediates rolling of human neutrophils on P-selectin, J. Cell Biol. **128**, 661 (1995).
[53] See Supplemental Material at http://link.aps.org/supplemental/10.1103/PhysRevFluids.4.063101 for the animations of leukocyte rolling at shear rates of $\gamma = 100\ \mathrm{s}^{-1}$ and $300\ \mathrm{s}^{-1}$.
[54] C. Sun and L. L. Munn, Particulate nature of blood determines macroscopic rheology: A 2-D lattice Boltzmann analysis, Biophys. J. **88**, 1635 (2005).
[55] C. Sun and L. L. Munn, Influence of erythrocyte aggregation on leukocyte margination in postcapillary expansions: A lattice Boltzmann analysis, Physica A **362**, 191 (2006).
[56] M. M. Dupin, I. Halliday, C. M. Care, L. Alboul, and L. L. Munn, Modeling the flow of dense suspensions of deformable particles in three dimensions, Phys. Rev. E **75**, 066707 (2007).
[57] M. M. Dupin, I. Halliday, C. M. Care, and L. L. Munn, Lattice Boltzmann modeling of blood cell dynamics, Intl. J. Comput. Fluid Dyn. **22**, 481 (2008).

[58] L. L. Munn and M. M. Dupin, Blood cell interactions and segregation in flow, Ann. Biomed. Eng. **36**, 534 (2008).
[59] D. D'Humières, I. Ginzburg, M. Krafczyk, P. Lallemand, and L.-S. Luo, Multiple-relaxation-time lattice Boltzmann models in three dimensions, Philos. Trans. A **360**, 437 (2002).
[60] C. Pan, L.-S. Luo, and C. T. Miller, An evaluation of lattice Boltzmann schemes for porous medium flow simulation, Comput. Fluids **35**, 898 (2006), proceedings of the First International Conference for Mesoscopic Methods in Engineering and Science.
[61] Z. Guo, C. Zheng, and B. Shi, Discrete lattice effects on the forcing term in the lattice Boltzmann method, Phys. Rev. E **65**, 046308 (2002).
[62] Z. Guo and C. Zheng, Analysis of lattice Boltzmann equation for microscale gas flows: Relaxation times, boundary conditions and the Knudsen layer, Intl. J. Comput. Fluid Dyn. **22**, 465 (2008).
[63] P.-O. Persson and G. Strang, A simple mesh generator in Matlab, SIAM Rev. **46**, 329 (2004).